Interstage Flow Interactions and Loss Generation in a Two-Stage Shrouded Axial Turbine

L. Porreca[1]
e-mail: luca.porreca@ch.manturbo.com

A. I. Kalfas

R. S. Abhari

Turbomachinery Laboratory,
Swiss Federal Institute of Technology ETH Zürich,
Zurich 8005, Switzerland

Y. I. Yun

S. J. Song

School of Mechanical and Aerospace
Engineering,
Seoul National University,
Republic of Korea

The aerodynamics and kinematics of flow structures, including the loss generation mechanisms, in the interstage region of a two-stage partially shrouded axial turbine are examined. The nonaxisymmetric partial shroud introduces highly three-dimensional unsteady interactions, the details of which must be understood in order to optimize the design of the blade/shroud. Detailed measurements of the steady and unsteady pressure and velocity fields are obtained using a two-sensor fast response aerodynamic probe and stereoscopic particle image velocimetry. These intrusive and nonintrusive measurement techniques yield a unique data set that describes the details of the flow in the interstage region. The measurements show that a highly three-dimensional interaction occurs between the passage vortex and a vortex caused by the recessed shroud platform design. Flow coming from the blade passage suddenly expands and migrates radially upward in the cavity region, causing a localized relative total pressure drop. Interactions of vortex and wake structures with the second stator row are analyzed by means of the combination of the measured relative total pressure and nondeterministic pressure unsteadiness. The analysis of the data gives insight on unsteady loss mechanisms. This study provides improved flow understanding and suggests that the design of the blade/shroud and second stator leading edge may be further improved to reduce unsteady loss contribution.
[DOI: 10.1115/1.2948961]

Introduction

The flow within a multistage axial turbomachine is inherently unsteady and turbulent due to the interaction of wakes and secondary flow structures, shed by upstream blades, with the downstream blades. Furthermore, the incoming wakes are chopped by the rotor blades, and then diffuse and deform as they pass through the nonuniform pressure field in the rotor passage. These unsteady phenomena affect the performance of the airfoils and generate noise and structural vibration. An improved understanding of the unsteady flow physics is still a critical issue in rotating turbomachinery design and is thus a key requirement in achieving further improvements in performance.

Previous experimental studies that examined flow interactions have used miniaturized fast response aerodynamic probe (FRAP) devices (Schlienger et al. [1], Miller et al. [2], Pfau et al. [3], Gaetani et al. [4]) to measure unsteady pressures and derive as well other flow field parameters. Recently, optical techniques such as particle image velocimetry (PIV) have also been applied to rotating machinery. However this measurement technique is still a challenge in such an environment because of the difficult optical access and the need to use a uniquely defined calibration procedure to take into account the image distortion due to the cylindrical shape of the window. Moreover, since PIV measures the velocity field of tracers that are added to the flow, achieving a uniform seeding with an optimum concentration is crucial. In large scale rotating turbomachinery research facilities, these issues are very critical.

For these reasons, there are not many publications regarding the successful application of PIV to turbomachinery. Wernet [5], Balzani et al. [6], Sanders et al. [7], Uzol et al. [8], Ibaraki et al. [9], and Estevadeordal et al. [10] studied the 2D steady and transient

flow fields in axial and centrifugal compressors. Liu et al. [11] and Göttlich et al. [12] made stereoscopic PIV measurements focusing on the wake-wake interaction at midspan in an axial transonic turbine and in the tip region of an axial compressor, respectively.

In the present work, extensive measurements using FRAP and stereoscopic PIV are made in a two-stage shrouded axial turbine. The investigation is focused on the flows within the interstage region. Partial shrouds are currently in use in some stationary industrial applications (Dorris et al. [13], Tomita [14], and Nirmalan and Bailey [15]), and they are receiving more attention due to the aerodynamic advantage of shrouded configuration as well as reducing thermal load and mechanical stress on the blade root (Harvey and Ramsden [16]; Willer et al. [17]). However, the optimal compromise between mechanical issues and aerodynamic performances is still an open issue due to the resulting highly three-dimensional unsteady flow field, difficulty in achieving an optimal cooling and severe heat load on the shroud sealing fins. The coupling between flow kinematics and loss generation is therefore investigated in order to gain a better understanding of the flow physics and to suggest ways to improve aerodynamic design of the blade/shroud components.

Experimental method

Research Facility. The experimental investigation has been performed in the research turbine "Lisa" at the Turbomachinery Laboratory of the ETH Zurich. The facility can accommodate a maximum of two stages of an axial turbine. The air loop is quasiclosed type (open to the atmospheric conditions) and thus includes a radial compressor, a two-stage water to air heat exchanger, and a calibrated Venturi nozzle for accurate mass flow measurements. A dc generator absorbs the turbine power and controls the rotational speed of the turbine shaft. The first and second rotors are mechanically decoupled by use of a twin spool shaft design. A pair of independent torque meters allow the torque of each rotors to be separately measured. To achieve the same rotational speeds, the shafts are coupled again before the DC genera-

Table 1 Main parameters of Lisa two-stage axial turbine research facility

Rotor speed (rpm)	2625
Overall pressure ratio	1.38
Mass flow (kg/s)	10.65
Blade count (stator/rotor)	42/42
Aspect ratio	1.8
Mach number (stator/rotor)	0.35/0.1
Reynolds number (rotor) based on C_{ax}	2×10^5
R_{hub}/R_{tip}	0.77
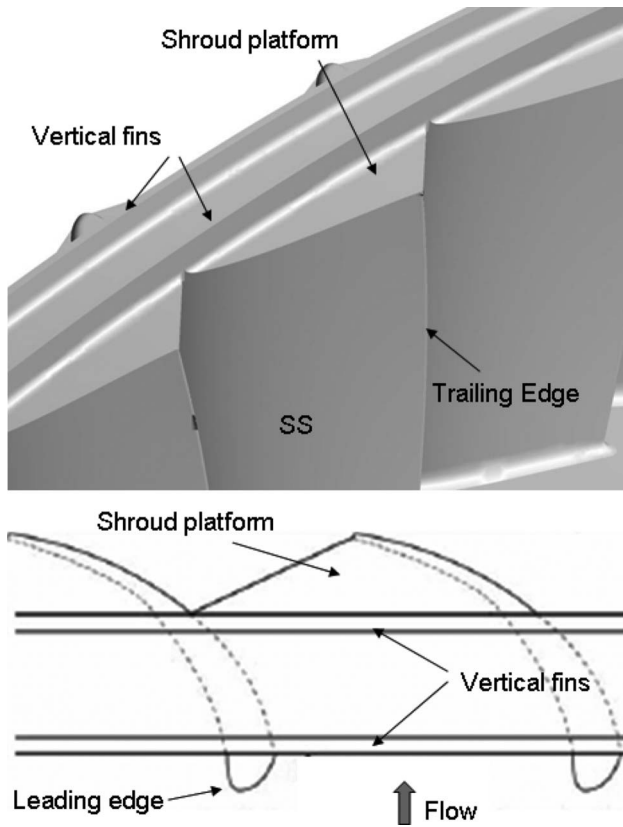
Fig. 1 Schematic of the rotor partial shroud geometry

Fig. 2 Optical windows and probe holes in the test turbine

tor. More details can be found in Porreca et al. [18].

The turbine's design allows quick and precise assembly and easy access to the measurement planes. The facility is equipped with a four-axis numerically controlled positioning system with high precision (± 0.05 mm in the radial direction and ± 0.002 deg in the yaw and circumferential angles). The turbine is normally operated at constant pressure difference across the stages. The turbine entry temperature is controlled to an accuracy of 0.3% and the shaft speed is kept constant by the dc generator within the range of $\pm 0.02\%$ (± 0.5 rpm). The main operational parameters of the facility are listed in Table 1. The test case under investigation is representative of a partially shrouded axial turbine for power generation applications and is sketched in Fig. 1. The partial shroud has two vertical fins and a shroud platform with cutbacks at the leading and trailing edges. The tip clearance in both rotors is 1% of the blade span.
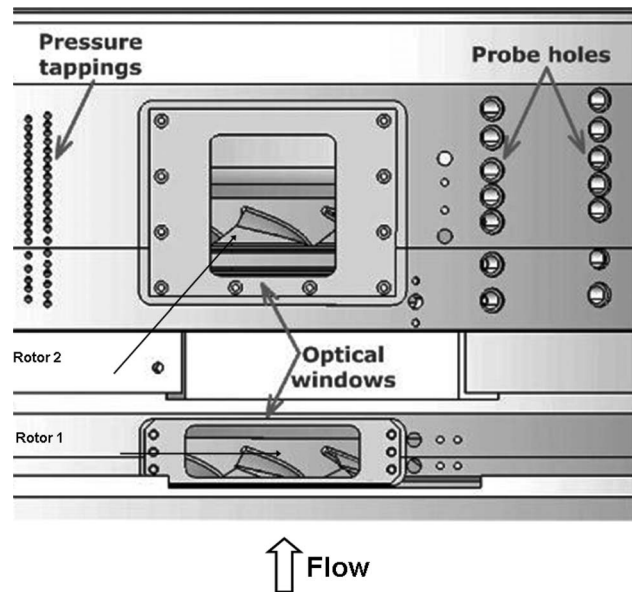
Measurement Techniques

Stereoscopic PIV. The two-stage axial research turbine rig Lisa has been equipped with a 3D-PIV optical measurement system. The stereoscopic PIV method is used to compensate for perspective errors (Prasad [19]) as well as to observe the highly three-dimensional flows. Two optical windows made of acrylic polymethyl methacrylate (PMMA) are installed in the test turbine, as shown in Fig. 2. The window surfaces have been carefully polished to achieve good transparency. The first window is located between the first rotor and the second stator, and the second window is downstream of the second rotor. The windows are designed to reproduce the exact shape of the double curvature contour in the casing of the inner wall. The flow was seeded with fine oil dioctylsebacat $C_{26}H_{50}O_4$ (DEHS) particles generated by a Laskin nozzle (Kähler et al. [20]). To obtain a uniform concentration an injection device was designed to seed the entire air mass flow. The injection location was selected at the outlet of the radial compressor and upstream the heat exchanger to guarantee a sufficient mixing between the flow and the seeding particles. Deposits of seeding material on the casing windows were not significant during the operation of the turbine. The nominal particle diameter was around 1 μm, which is considered adequate (according to Mellin [21]) for a frequency response up to 10 kHz.

The digital images are recorded with 1280×1024 pixels 12 bit charge coupled device (CCD) cameras (PCO SensiCam SVGA). The pixel size and pitch are 6.7×6.7 μm^2 and 9 μm, respectively. The cameras are set, taking into account the Scheimpflug condition (Zang and Prasad [22]). Nikon AF Micro Nikkor lenses with a focal length of 60 mm are used for camera optics. A double-cavity (Nd:YAG) laser (Solo120PIV, New Wave Research) is used as a light source. The laser generates a maximum energy of 120 mJ/pulse of 532 nm wavelength green visible light. The pulse width is 10 ns, and the repetition rate is 15 Hz. The bursts of laser light are synchronized with cameras via a Dantec FlowMap system hub. The laser beam is delivered to a laser endoscope (Intelligent Laser Applications (ILA)) through an articulated mirror arm. The laser endoscope both generates the laser sheet through a cylindrical lens and bends the laser sheet by 90 deg through a prism in its tip. The outer diameter of the laser endoscope is 8 mm, and the divergence angle of the laser sheet is approximately 16 deg. The cameras and laser endoscope are mounted on a motor-controlled one-axis linear stage so that cameras and the light sheet can be moved together in the radial direc-
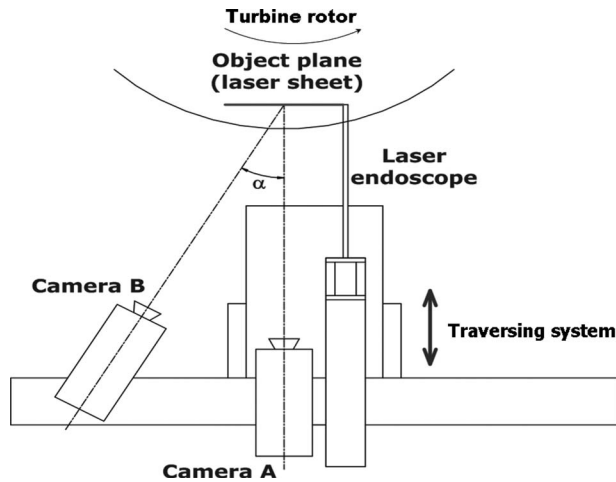
Fig. 3 Stereoscopic camera configuration in the test turbine

Fig. 5 Recorded image of seeded flow in the interstage measurement region

tion (Fig. 3).

By traversing radially, several blade-to-blade planes can be illuminated with the laser endoscope. Camera A is positioned such that its axis is perpendicular to the light sheet plane to avoid an interference with the laser endoscope. Camera B is tilted by different angles (α=22 deg, 25 deg, and 30 deg), as shown in Fig. 3. The image plane (CCD plane) of Camera B is further rotated by 5 deg to satisfy the Scheimpflug condition, which ensures that all particles in the object field will be in good focus in the image plane (Prasad [19]). To compensate for the perspective distortion of the field of view due to the tilt angle of Camera B as well as the optical distortion through the double-curvature windows, a three-dimensional calibration method is used.

However, in the interstage area, the window has an abrupt change of curvature, which results in a severe optical distortion that could not be corrected by the calibration procedure. Therefore, data measured in this region are blanked out. The details of the calibration method can be found in Soloff et al. [23], while the description of the calibration procedure applied for these measurements is reported in detail in Porreca et al. [24].

Figure 4 shows the FRAP and five hole probe (5HP) measurement planes and the region of PIV measurements at the interstage and at the turbine exit region. The first stator is not shown in the figure in order to better highlight the measurement areas. Regarding the interstage region, measurements were taken in 15 blade-to-blade planes from 66% to 97%. One blade passing period is divided into 20 time steps, and between 60 and 100 digital image pairs are recorded for each measurement plane at each time step of a 50×40 mm^2 area. For the downstream region, measurements are made on three planes inside the shroud cavity and 17 blade-
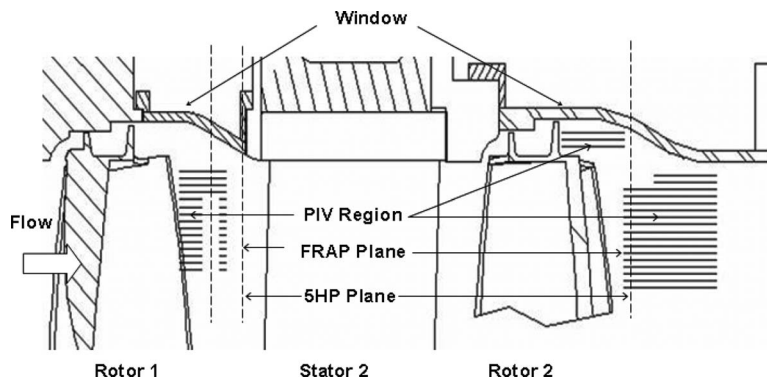
to-blade planes (from 60% to 96%) downstream of the second rotor. One blade passing period is divided into ten time steps, and 100 image pairs are recorded on each plane at each time step. The time interval between two laser bursts varies between 2 μs and 4 μs depending on the average flow field velocity. Each pair of images is interrogated using a cross-correlation analysis of 32 $\times 32$ pixel subareas with an overlap of 50% between adjacent interrogations. An advanced interrogation method of window offset is used (Westerweel et al. [25]; Scarano and Riethmuller [26]). The theoretical analysis and simulations performed by Westerweel [27] show that the signal-to-noise ratio for PIV measurements with window offset is approximately three times larger than that without window offset when the flow has high turbulence intensity. Furthermore, the method of window offset is effective in reducing the error due to loss of pairs. To filter out spurious data, a criterion based on the local median is used (Westerweel [27]). Figure 5 shows a typical recorded image in the interstage measurement region. Visible in the picture are the blade trailing edge, the shroud platform, and the seeding particles that have been illuminated by the laser sheet.

Uncertainty Analysis of PIV Measurements. For the estimation of the uncertainty in the PIV velocity measurements, many parameters have to be considered (Raffel et al. [28]; Willert and Gharib [29]). These include

- particle image diameter
- displacement of the particle relative to the size of the interrogation area
- particle image density
- local velocity gradients
- out-of-plane motion of tracer particles
- background noise

There is no established method to analytically evaluate the uncer-

Fig. 4 Measurement regions: PIV, FRAP, and 5HP

Table 2 Uncertainty analysis of stereoscopic PIV measurements

Span		Velocity (m/s)			
		Tangential velocity	Axial velocity	Radial velocity	Yaw angle
		Interstage region			
96%	Actual values	30	−5	10	80.54
	Mean	28.31	−3.91	8.31	82.16
	Standard deviation (m/s)	0.92	0.71	2.47	1.30 deg
	Bias error (m/s)	1.7	−1.09	1.7	−1.63 deg
66%	Actual values	30	65	10	24.7
	Mean	28.32	62.99	16.59	24.22
	Standard deviation (m/s)	2.25	2.69	5.97	1.92 deg
	Bias error (m/s)	1.68	2.01	−6.59	0.55 deg
		Turbine exit region			
85%	Actual values	10	30	5	18.43
	Mean	13.09	31.10	1.08	22.83
	Standard deviation (m/s)	1.99	3.48	0.59	3.31 deg
	Bias error (m/s)	3.09	1.10	−3.92	4.40 deg

tainty in PIV measurements due to the above factors. Therefore, the assessment of PIV accuracy may be done for each PIV system by using one of the following three methods. The first method is to make PIV measurements in a flow field with an exact solution (e.g., Poiseuille flow or three-dimensional rotating disk flow) and then evaluate uncertainty for the flow field. However, it is difficult to guarantee that the uncertainty determined in a canonical flow field can be applied to other more general flow fields. Also, it is not always possible to introduce such canonical flows with exact solutions in a specific environment such as the current test rig. The second method is to conduct a Monte Carlo simulation of particle displacements (Keane and Adrian [30]; Raffel et al. [28]). This approach allows the uncertainty of PIV measurements in a broad range of flow fields to be assessed. Third, PIV results can be compared against data obtained with hot wire or pneumatic probe methods or from direct numerical simulation (Scarano and Riethmuller [26]). However, a rigorous evaluation of uncertainty is difficult with this method since the measurement techniques are different and the direct numerical simulation itself has uncertainties.

In the current investigation, a Monte Carlo simulation has been conducted to evaluate measurement errors of PIV. To carry out a Monte Carlo simulation, tracer particle images must be artificially generated. The light intensity scattered from individual tracer particles is assumed to have a Gaussian profile in both the in-plane (x, y) and out-of-plane (z) directions,

$$I(x,y,z) = I_0 \exp\left[\frac{-(x-x_0)^2 - (y-y_0)^2}{(1/8)d^2}\right] \exp\left[-\frac{z_0^2}{(1/8)\Delta z_0^2}\right] \tag{1}$$

The location of each tracer particle (x_0, y_0, z_0) is set by using a random number generator. Then, the light intensity scattered from the particle at each location in an interrogation area can be defined from Eq. (1). Four parameters—particle image diameter, number of particles, maximum light intensity I_0, and actual displacement—must be given a priori. The diameter of tracer particles is set such that the particle fills a 2×2 pixels pixel or 3×3 pixels pixel region. The number of particles used here is 50. Both of these parameters were determined via a trial-and-error process so that the artificially generated images look similar to the measured images. Based on these artificial images, the first and second image frames with a time interval between 2 μs and 4 μs can be generated. The actual displacements of the particle $(\Delta x, \Delta y, \Delta z)$ are taken from a representative averaged velocity value measured with PIV at each point of interest. Based on these displacements, the image pairs of tracer particles in the object

plane can be generated.

The images are not generated for the entire field of view (for the current investigation, 50×40 mm^2) but at three points (as shown in Table 2). A point in the field of view corresponds to a 32×32 pixel interrogation area in the image plane. However, the images are generated in a 96×96 pixel pixel region to properly account for the particles that enter and exit the 32×32 pixel interrogation area that is located at the center of the 96×96 pixel pixel region. With stereoscopic PIV, the displacement values seen by the two cameras are different, particularly when there are out-of-plane displacement components. Also, perspective and optical distortions of the images occur when the particle images are projected onto the image planes. The calibration procedure is used to estimate both the image distortion and the displacements seen in both cameras' image planes. The interrogation area is also subject to background noise due to reflection on solid surfaces and the light that is scattered from tracer particles located outside the light sheet. Therefore, the background noise has a static intensity level (from the reflection) as well as a randomly moving pattern (from the scattering of particles outside the light sheet). To obtain a spatially random intensity pattern, a random number generator has been used. Then, the background noise is superimposed on the particle images. Because there is a randomly moving pattern in the background, the noise patterns for the first and the second frames are separately generated. Three hundred particle image pairs for each point are generated to carry out statistical evaluations. The stereoscopic PIV error is then evaluated by comparing the imposed displacements to the displacements calculated from the artificially generated images. The measurement error consists of two parts, *bias error* and *root-mean-square (rms) error* (Raffel et al. [28]),

$$\varepsilon_{\text{PIV}} = \varepsilon_{\text{bias}} + \varepsilon_{\text{rms}}$$

The bias error is defined as the difference between the actual velocity value and the averaged value measured with PIV. This bias error originates from loss of pairs and velocity gradients in the interrogation areas.

rms error is the standard deviation of the values measured with PIV and can be regarded as measurement uncertainty of PIV. Table 2 shows the results of the uncertainty analysis expressed in terms of the bias and rms errors at the interstage and turbine regions. The bias error at the interstage region for the axial and tangential velocities (in-plane components with respect to the laser light sheet) is always in the range of ±2 m/s. Standard deviation is in the lower range of 4–7% and higher close to the tip

Table 3   Uncertainty in measurements of 5HP and FRAP

Probe type	φ (deg)	β (deg)	P_t (Pa)	P (Pa)	Ma
5HP	0.3	0.3	60	130	0.4%
2S-FRAP	0.3	0.3	100	150	0.5%

where the absolute velocity magnitude is smaller. In the turbine exit region, the magnitudes of the bias errors are similar, but the rms errors are larger.

The bias error of the radial velocity (out-of-plane component) is more than 10% in all the planes; therefore, the radial velocity measurements ought to be assessed only qualitatively. Another trend is that the errors of the in-plane components (tangential and axial velocities) are similar for all three locations while the error of the out-of-plane component increases as the measurement location is farther from the optical window. Measurement planes farther from the window suffer from more severe optical distortion. Thus, the error of the out-of-plane component appears to be more susceptible to optical distortion.

FRAP and 5HP. Flow parameters, including total and static pressures, flow angles, velocity components, and Mach numbers, are measured at frequencies of up to 40 kHz using a two-sensor FRAP. This probe is a modified version of the conventional single sensor probe; a second sensor that is sensitive to pitch angle variations of the flow is incorporated. This two-sensor FRAP has been used in previous investigations (Porreca et al. [31]). The FRAP also provides unsteady temperature measurements at a low frequency of up to 10 Hz. The absolute uncertainties in the measurements are listed in Table 3. Temperature measurements obtained with FRAP have an absolute uncertainty of the order of ± 0.3 K.

The FRAP probe has been developed in the Turbomachinery Laboratory at ETH Zurich in the last 20 years of research. Time resolved measurements have been compared with laser Doppler velocimetry measurements taken at the exit of a centrifugal compressor facility [32]. The agreement of the time mean velocities was found in the range of 0–4% while the time resolved velocities were within 2–5%. Furthermore, acomparison with nonintrusive measurements is presented in this paper. An additional comparison between FRAP and pneumatic probe can be found in Refs. [33,18]. In the latter publication, the FRAP and 5HP data are compared at the exit of the first rotor and second stator of an axial turbine with exactly the same blade profile geometry of the one employed in the current work. The comparison shows that the pneumatic averaged data lay always in the minima and maxima of the FRAP measurement and therefore confirms the accuracy of this measurement technique.

The measurement grid comprises 1502 points that are distributed uniformly in the circumferential direction at every 3.5% pitch (32 points in a pitch range of 1.1) and 47 points clustered toward the end walls in the radial direction. Data from the sensors are sampled at 200 kHz, which corresponds to 109 samples for each blade passing period. Phase-locked averaging of the data is done over 80 rotor revolutions.

Steady state measurements are performed using miniaturized pneumatic 5HPs with a 0.9 diameter cobra head shape (Treiber et al. [34]). The probe is calibrated for ranges of ± 14 deg in yaw and ± 30 deg in pitch angle. The uncertainty of pneumatic probe measurements is reported in Table 3 for angles of ± 10 deg in yaw and ± 10 deg in pitch. For higher pitch angles, higher uncertainty is detected.

FRAP–3D PIV Comparison and Analysis

Figure 6 shows a comparison between the velocity measured by the 3D PIV (Fig. 6(a)) and the FRAP (Fig. 6(b)) data. The FRAP data are presented over the same region as the PIV measurements. Regions of the PIV measurements that have insufficient laser illumination are blanked out at the left and right borders. Both data sets are presented with the same scale and levels. The higher tangential velocity region in the middle of the pictures shows the presence of the tip passage vortex that is located between 0.8 and 0.9 of the span height. The comparison shows good agreement between the two measurement techniques. In the PIV plot, the core with a high tangential velocity is slightly larger compared to the FRAP measurements. However at the location of the vortex core the differences in absolute magnitudes of velocity are comparable and are within the range of ± 1.5 m/s, which is comparable to the uncertainty of the PIV measurements as discussed in the previous section.

Figure 7 shows the pitchwise yaw angle distribution at different axial planes downstream of the second rotor blade. The time averaged FRAP and PIV data are presented together with 5HP measurements. The FRAP and 5HP measurements are made in the plane located at 153% of tip C_{ax}. At this plane, there are blanked out regions in the PIV data, and thus three other planes located at 171%, 196% and 208% tip C_{ax} are presented for the PIV data.

A good agreement between the probe and the optical measurement techniques is again observed. An underturning/overturning behavior is observed from a 0.7 span up to the blade tip where the blade profile is designed to align the flow with the underturned leakage flow in order to minimize mixing losses. The yaw angle profiles measured with the probes (FRAP and 5HP) are in good agreement up to a 0.75 span. Discrepancies are observed from the 0.75 span up to the blade tip since the passage vortex in the region generates a high level of unsteadiness, which results in the time averaged signal of the fast response probe being different from the pneumatically averaged signal of the 5HP.

Overall the time averaged PIV data are in good agreement with the probe data. Differences are of the order of ± 2.5 deg in the region from 0.6 up to 0.9 blade span. The largest differences are in
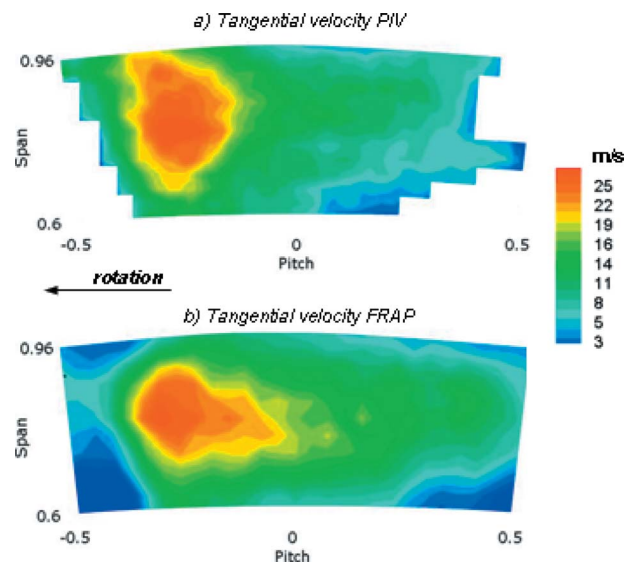

Fig. 6   Measured absolute tangential velocity at one rotor blade position: (a) PIV and (b) FRAP—turbine exit region
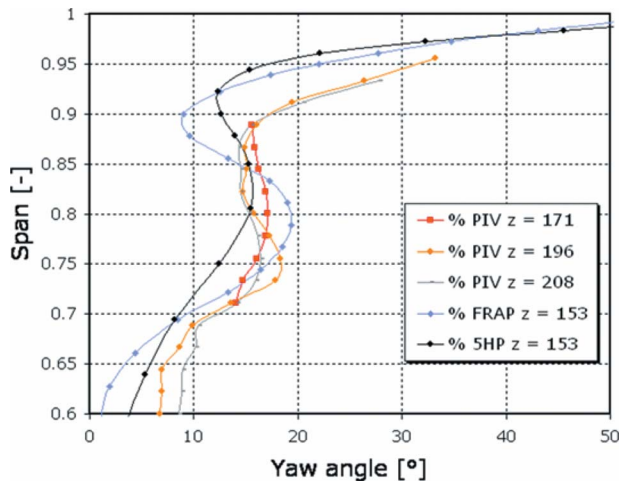
Fig. 7 Comparison between FRAP, 5HP, and PIV time averaged pitchwise yaw angles—turbine exit region

the vicinity of the passage vortex core, where perhaps the errors in the out-of-plane velocity component in the PIV data contribute to the observed differences.

Above a 90% span, in the region of overturning due to the leakage layer, the trend in the probe data is captured correctly by the PIV, but there are larger differences compared with the probe data. The PIV data appear to be displaced away from the blade tip. This is expected as the PIV data are measured further downstream of the blade row (171–208% tip C_{ax}) compared to the probe data that are measured at 153% tip C_{ax}. At the more downstream positions the leakage flow is entrained more into the main flow.

Interstage Flow Analysis

Figure 8 shows the absolute yaw angles downstream of the first rotor blade. These PIV measurements are averaged in time and pitch and presented for axial planes located between 109% and 128% midspan C_{ax}. The passage vortex produces large flow underturning, and this is evident in all the measurement planes between 70% span and the tip. Further downstream, an increasing region of underturning is observed in the tip region due to the incoming tip leakage flow. Within the labyrinth seal, the flow retains its relatively high tangential momentum that has been im-
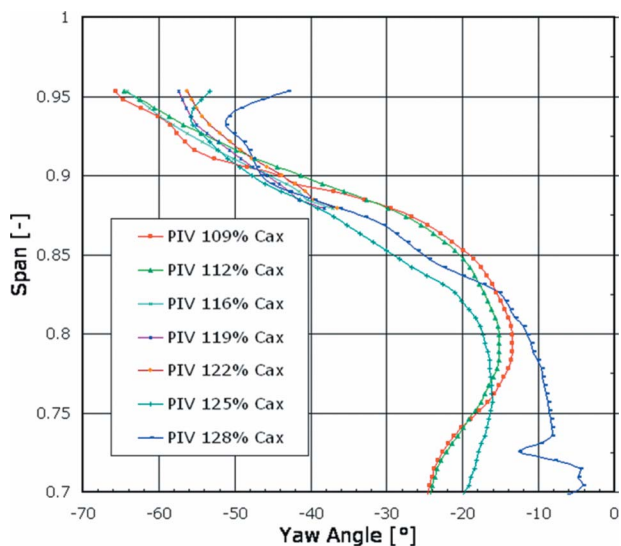

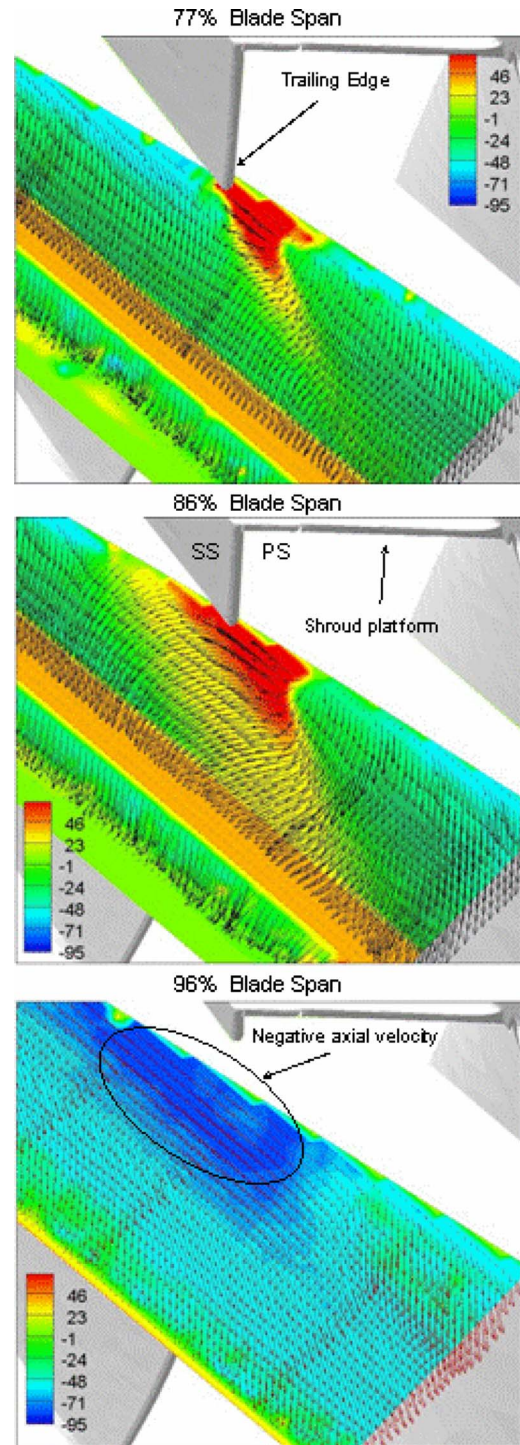**Fig. 8 PIV measured time and pitchwise averaged absolute yaw angles at different axial planes**

Fig. 9 PIV measured absolute yaw angles at different tangential planes. Vectors show the in-plane velocity component—interstage region.

parted by the upstream nozzle guide vanes (NGVs) Therefore at the rotor exit, there is a relatively high difference in the tangential momentum of the main stream and the leakage flow. This difference in momentum increases the mixing losses, and it is for this reason that some designs adopt "bladelets" to turn the leakage flow in order to reduce the difference in tangential momentum and thus minimize the mixing losses. These devices have been found to be more effective when placed in the stationary frame (Rosic and Denton [35]) compared to the shroud (Wallis et al. [36]).

Figure 9 shows contour plots at three blade span positions of

the PIV measured yaw angle. Superimposed on the contour plots are vectors of the in-plane velocities. The contours in the middle of the measurement plane are blanked out, as shown in the orange region with zero length vectors; these PIV data are unusable due to the optical distortion through the window. All the measurements are derived from phase-locked data, which are averaged over 100 samples. At the 77% blade span plane, the measured yaw angle shows two distinct regions: the main "undisturbed" flow in the middle of the passage and the wake region that is close to the trailing edge. In the wake region the flow is underturned with yaw angles as large as 80 deg; the deficit in the axial velocity and the presence of the passage vortex cause this underturning. The wake region is highly confined, compared to the main flow, and thus there are large circumferential gradients in the yaw angle.

At the 86% and 96% blade span positions, the influence of the wake is reduced. At the 86% position, the region of underturned flow is significantly reduced compared to that at the 77% blade span position. At the 96% blade position, no region of underturned flow is observed. Rather the passage vortex results in a region with both strong overturning of the flow and measured negative axial velocities. The resultant yaw angles exceed 90 deg in this region. The negative velocities arise due to the rapid flow expansion as the shroud platform uncovers the blade passage. The passage vortex grows downstream of the blade throat and expands over the shroud platform. This growth and expansion results in an upward radial motion that is relatively weak in the middle of the blade passage and stronger downstream of the blade's trailing edge. A similar radial motion is observed in the leakage cavity that is downstream of the second rotor with a similar partial shroud geometry; these measurements in the cavity are detailed in Yun et al. [37].

Figure 10 shows contour plots of the PIV measured absolute yaw angles at two axial planes, 109% and 114% midspan C_{ax}. The in-plane velocity vectors are superimposed on the contour plots. The vertical dashed line shows the trailing edge of the rotor blade projected onto these downstream planes. The rotor motion is from right to left. In order to highlight the wake and secondary flow, only half of the blade pitch region is shown. The yaw angle varies between −80 deg and +40 deg due to the presence of the passage vortex. In the region between the 80% span and the blade tip, these variations result in large gradients of the yaw angle.

These gradients are larger closer to the blade (109% mid C_{ax} compared to 114% mid C_{ax}) since the mixing weakens the passage vortex as it evolves downstream.

The in-plane velocity vectors show the presence of a vortex at the trailing edge of the rotor blade. Its vorticity is of opposite sign to that of the passage vortex. This flow phenomenon is sometimes observed in turbomachinery blade flows and has been previously observed in a study of low aspect ratio, high turning NGVs (Pullan et al. [38]). The rotation of this observed vortex is consistent with the shedding of streamwise vorticity from the pressure side to suction side at the blade's trailing edge. The partial covering of the shroud platform decreases the blade loading on the blade tip and thus enhances the shed vorticity.

A combined effect of the passage vortex and the TE shed vortex is to displace the underturned low momentum flow toward the suction side. A comparison of the yaw angles in the upstream (109% mid C_{ax}) and downstream (114% mid C_{ax}) planes shows that the gradients in the yaw angle are substantially reduced. This is a result of the merging of the two vortices. The merging and subsequent dissipation of the vortical structures result in mixing losses that may be quantified in terms of the relative total pressure coefficient. This is accomplished from the FRAP measurements in the axial plane located downstream at 152% mid C_{ax}, as shown in Fig. 11.

Figure 12 shows a contour plot of the measured relative total pressure coefficient. The data are phase locked at a rotor blade position of $T/T_0 = 1.85$. The projected locations of the rotors' trailing edge are shown by the dashed lines, and the pressure and
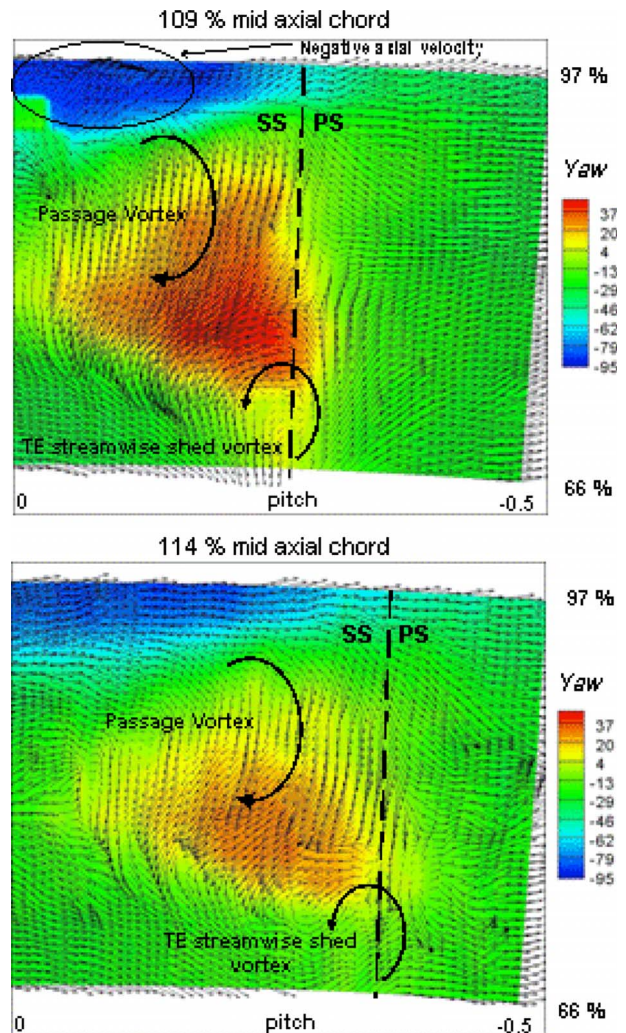

Fig. 10 PIV measured absolute yaw angles at different axis-perpendicular planes. Vectors show the in-plane velocity component—interstage region
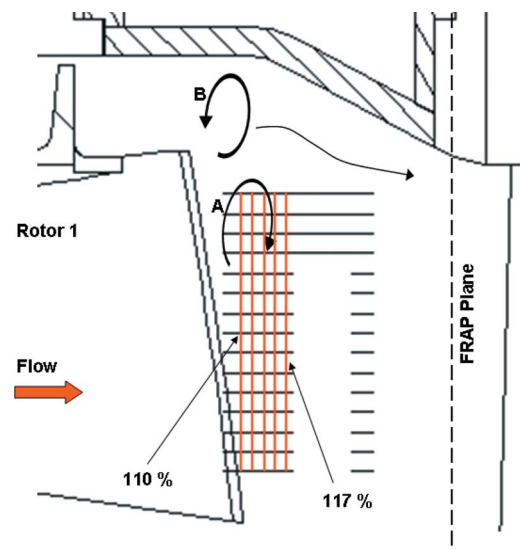

Fig. 11 Schematic of flow structures and measurements in the interstage region
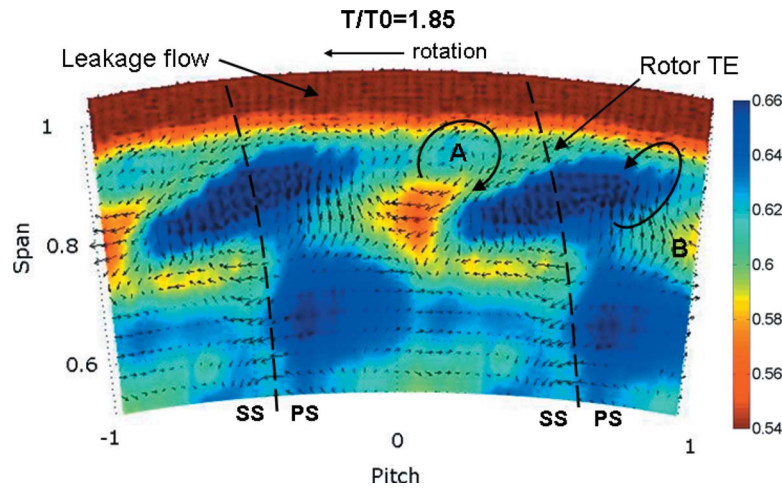
Fig. 12   FRAP measurements of the relative total pressure coefficient Cpt_{rel} and secondary flow vectors—interstage region

suction sides are also identified. Superimposed on the contours are vectors of the local secondary flow velocities. The secondary flow velocity computed at each time step is defined as

$$\vec{u}_{\sec} = \vec{u}_i - (\vec{e}_{mean}\vec{u}_i)\vec{e}_{mean}$$

where $\vec{u}_i$ is the local flow vector and $\vec{e}_{mean}$ is the circumferentially averaged mean unit vector. The contour plot shows that the total pressure is reduced in the wake region, downstream of the rotor's trailing edge, and in a circumferential region (0.95–1.05% blade height) that is associated with the cavity flow. Two counter-rotating structures are visible from the velocity vector field. They are labeled as structures A and B in Fig. 12 and can be seen to push low momentum fluid from the wake toward the suction side of the blade. The vortex that was shed from the rotor's trailing edge, and was identified in Fig. 10, is not seen in Fig. 12. A comparison of the PIV (Fig. 10) and FRAP (Fig. 12) data identifies structure A as the passage vortex and structure B as a vortex that originates from the sudden expansion downstream of the shroud cutback. A schematic of the flow structures is shown in the meridional view of the interstage region in Fig. 11. Also shown in the figure are the relative locations of the FRAP (vertical dashed line) and PIV (series of horizontal lines) measurements. Vortex B could not be observed in the PIV data since the measurement region does not extend above 96% span. However, this vortex is entrained into the main flow downstream of the PIV measurement region and seen in the FRAP plane. Evidence of this structure can be seen from the measured data in the cavity downstream of the second rotor, as described in Yun et al. [37].

In Fig. 13 the time evolution of the relative total pressure coefficient is plotted as a function of the measurement position with respect to the stator blade. The vertical dashed lines denote the position of the leading edge of the second stator, and a blade passing fraction of $T/T0 = 1.85$ (which is used in Fig. 12) is shown by the horizontal dashed line. The contour levels in Figs. 12 and 13 are the same in order to facilitate the interpretation of the plots. The regions of reduced relative total pressure associated with the vortical structure described previously in Fig. 12 are seen to lie along inclined lines in Fig. 13. This inclination indicates that regions of lower total pressure move together with the rotor blade. At 76% span, Fig. 13(a), the degree of interaction with secondary flow is relatively high.

However, no substantial differences between the passage vortex A and the leakage vortex B are seen in Fig. 13. Rather only a broad region of decreased relative total pressure is observed. As the leading edge of the second stator is approached by the flow structures, the size of the region of low relative total pressure decreases. In Fig. 13(b) the time-distance diagram is presented for

the blade midspan location. At this position, no secondary flows are present and the flow field is dominated by the rotor wake and the potential field of the second stator. The rotor wake is shed at the trailing edge and is then convected downstream to impinge on the second stator blade row—first on the suction side of the blade and then on the pressure side of the following blade. As the wake passes through the passage of the stator (the middle of the passage corresponds to a stator pitch of approximately −0.4), there are very few disturbances. However, as the rotor is moving, the wake is periodically bowed and then compressed due to the potential field of the stator's leading edge.

The variation in the relative total pressure is higher for the passage vortex (Fig. 13(a))—note that the contour scales are the same in Figs. 13(a) and 13(b). In the region of interaction with the second stator leading edge (pitch=0.2), the time averaged relative total pressure coefficient deficit is about 6.6% with respect to the same averaged value at the pitch position equal to 0.6 where the wake is undisturbed. On the other hand, at 76% span the time averaged relative total pressure increase in this location is equal to 5.1% with respect to the position pitch=0.6. This concludes that in the case of the passage vortex (76% span), although variation is higher in the time domain, the variation of the relative total pressure in the second stator leading edge region is lower than in the wake.

At each measurement point the time dependent pressure can be written as

$$P(t) = \tilde{p}(t) + p'(t)$$

where $\tilde{p}(t)$ is the phase-locked measured pressure and $p'(t)$ is the nondeterministic part of the pressure signal. The pressure unsteadiness coefficient P_u is then defined as the ratio of the rms value of the term p' and the relative dynamic head,

$$P_u = \frac{\text{rms}(p')}{0.5\rho V_{\text{rel}}^2}$$

The rms value of p' is determined from 80 instantaneous samples. Figure 14 shows a P_u coefficient plotted in a time-distance diagram at 76% and mid span. The loss generation mechanism can be assessed from analysis of the phase-locked measured relative total pressure (Fig. 13) nondeterministic pressure unsteadiness P_u.

In Fig. 14(a), the levels of pressure unsteadiness are elevated in regions associated with the passage vortex, namely, the inclined lines that indicate the downstream convection of the passage vortex. When the passage vortex impinges on the leading edge of the second stator, the levels of pressure unsteadiness are significantly modulated and vary from 8% to 13%. On the other hand, in the
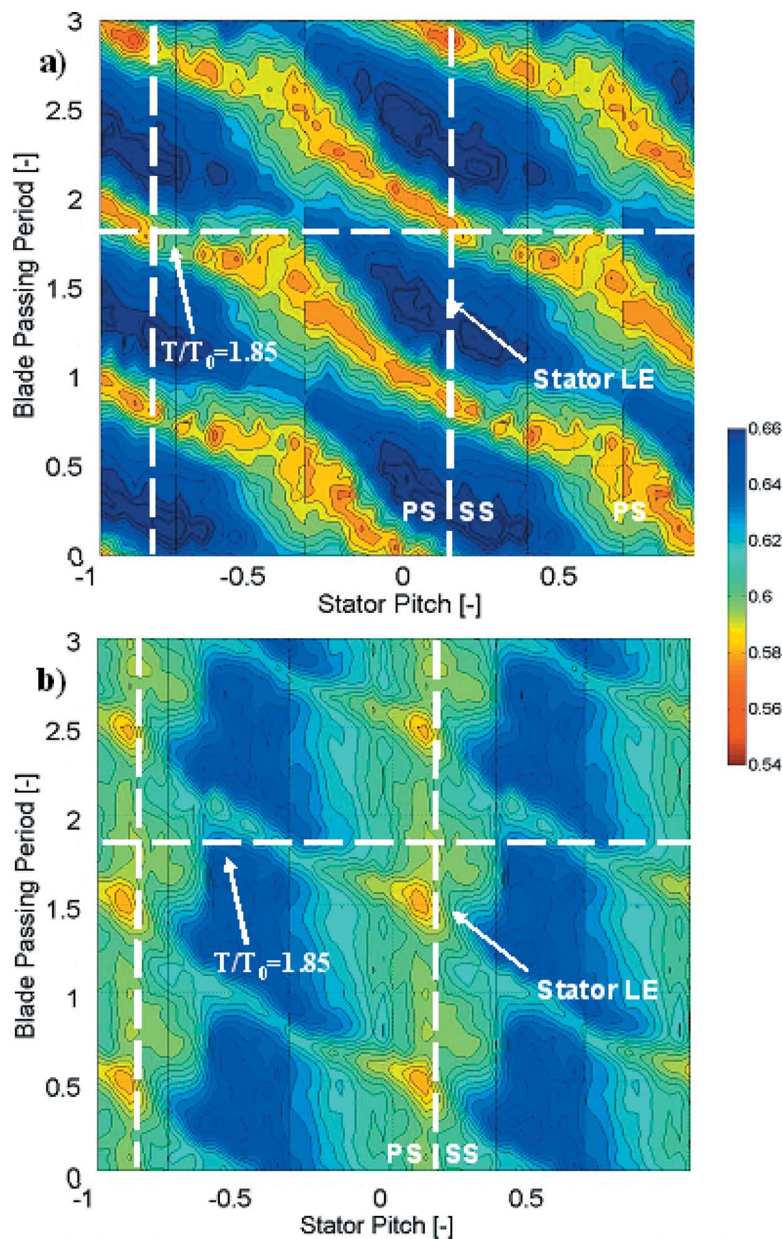
Fig. 13 Time-distance plot of relative total pressure coefficient Cpt_{rel} at (*a*) 76% span and (*b*) 50% span

regions where the main flow is dominant, P_u is as low as 2%. The effect of vortex stretching and growth when the passage vortex interacts with the second stator's leading edge can be observed. The stretching mechanism occurs when the vortex is accelerated in the stator passage, while vortex growth occurs due to the blockage effect of the potential field generated from the stator's leading edge. Within the stator passage (stator pitch of approximately −0.4) the levels of P_u are as high as 13%; however at the stator leading edge (stator pitch around 0.2) the level of unsteadiness reduces to around 8%.

In Fig. 14(*b*) the time-distance plot of the pressure unsteadiness coefficient for the midspan location is shown. The effect of the secondary flow is negligible at this span, and thus the levels of unsteadiness are significantly lower than that in Fig. 14(*a*). Nevertheless regions with relatively higher unsteadiness are associated with the rotor wake structure and are seen to lie along inclined lines. In these regions, the level of unsteadiness is as high as 4%, whereas in the main flow the peak values decrease to no

more than 1%. The trajectory of the rotor's wake, which is convected downstream through the passage of the second stator, can be inferred from the region of elevated P_u. When approaching the second stator's leading edge, the trajectory has a kink, which is also accompanied by a broad region of increased pressure unsteadiness.

A comparison of the relative pressure coefficient (shown in Fig. 13) and the pressure unsteadiness coefficient (Fig. 14) shows that regions of low relative total pressure coincide with the regions of high pressure unsteadiness both in the passage vortex region and in the wake region.

Since the measurement probe is in the stationary frame, i.e., fixed with the stator row, the relative total pressure varies (on the time and space domain) due to the combination of the rotor motion, the potential field created by the stator row, and the losses generated in the rotor flow passage. For this reason, losses cannot be isolated from the other effects. The quantification of loss can only be properly made by the measurement of entropy, which is
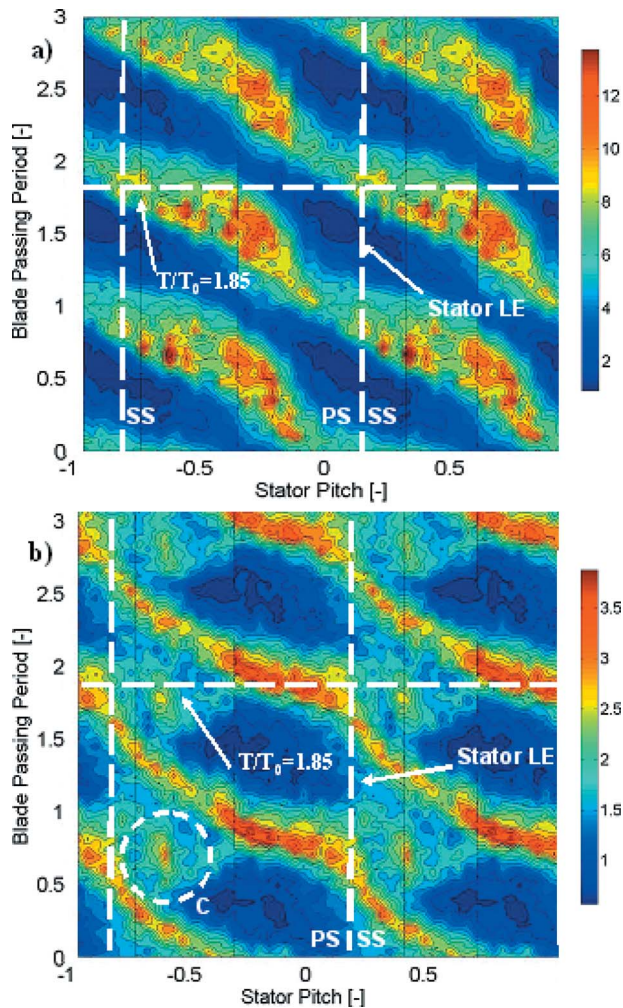
Fig. 14 Time-distance plot of pressure unsteadiness coefficient Pu (%) at (*a*) 76% span and (*b*) 50% span

Fig. 15 Circumferential evolution of yaw angle at different axial locations (110%–152% C_{ax}) at 80% span—one rotor blade position

retrieved by the combination of instantaneous temperature and pressure. Although the FRAP can measure both quantities simultaneously, the frequency response of the temperature signal is several orders of magnitude lower than the pressure signal; thus these data cannot be used for unsteady entropy measurements.

The set of measured data presented in this work clearly show a strong correlation between region of low relative total pressure and high nondeterministic pressure unsteadiness. The combination of these two quantities can be considered as an indication of loss production, and thus unsteady loss mechanisms can be assessed.

Kelvin's theorem indicates that the circulation around a stream tube is constant. Thus in an incompressible flow, such as that in the present work, an increase in the vortex diameter is accompanied by a decrease in the kinetic energy. This induces a lower dissipation and thus lower rate of mixing and loss generation. This phenomenon occurs periodically when the vortex diameter grows due to the blockage effect of the second stator leading edge and is clearly observed from the measurement of relative total pressure at 76% span (Fig. 13(*a*)) together with the increased level of unsteadiness in Fig. 14(*a*). A similar approach can be used in the analysis of the wake mechanism. If the wake is considered as a vortical structure with two counter-rotating vortex sheets, according to Kelvin's theorem, the velocity difference is increased when the wake is compressed. This compression therefore results in an increased velocity gradient inside the wake, which in turn results in an increase in the mixing losses. This process is shown in Fig. 13(*b*) around a pitch of 0.2 where a broad area of increased rela-
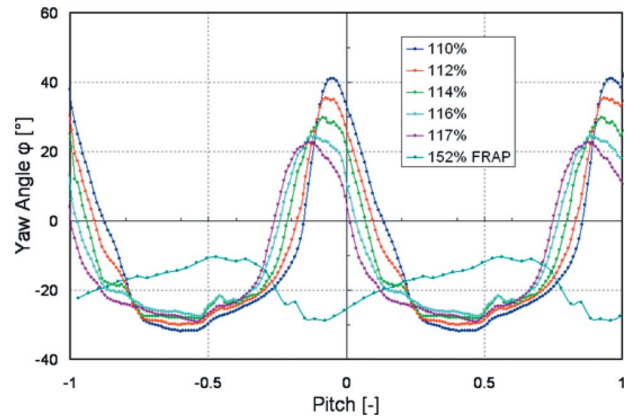
tive total pressure drop, as well as an increased level of pressure unsteadiness (Fig. 14(*b*)), is measured. Thus there is a clear link between the loss production mechanism and the kinking of wake's structure as the wake is turned and successively compressed around the stator leading edge.

It is also noteworthy to point out the concentrated region of high unsteadiness in the middle of the rotor blade passage—this is labeled as C in Fig. 14(*b*). Its periodic appearance suggests that it is associated with the chopped wake shed from the first NGV. This chopped wake is convected downstream through the rotor blade passage. Further analysis is required to confirm the source of this concentrated region since the equal number of blade counts does not make it possible to clearly separate the effect of flow structures generated in the NGV or in the rotor.

The measurements of the relative total pressure and pressure unsteadiness coefficients that were presented above show that the unsteady loss generation mechanisms at the midspan are different from those in the secondary flow region. In the region of secondary flow, the mechanisms are driven by the stretching and growth of passage vortex, and from the measured data, this mechanism is more pronounced at 76% span compared to the midspan region. Thus, modifications to the characteristics of the secondary flow deserve more attention in the aerodynamic design. For example, a rotor/stator design that increases the mixing in the tip region and thus reduces the diffusion of the unsteady vortex should improve the aerodynamic performance. This can be accomplished by including forward sweep in the blade stacking on the second stator's tip as a means to increase the axial distance between the rotor and stator.

The degree of mixing of the flow in the interstage region can be studied by observing the variation of the measured yaw angle at one fixed rotor blade position at different axial location in the volume shown in Fig. 11. The yaw angle variation, derived from the PIV measurements, as a function of the blade pitch is shown in Fig. 15 for five axial positions (from 110% C_{ax} to 117% C_{ax}). At all positions the data are measured at 80% blade span. Also shown in the figure is the yaw angle derived from the more downstream located FRAP. It can be seen that the largest changes in the yaw angle occur at the most upstream position (110% C_{ax}). The peak value occurs at a pitch of approximately −0.1, and significant underturning occurs in the pitch range of −0.15 to 0.1. At the more downstream positions, the peak value decreases and occurs at a more negative pitch as the passage vortex convects downstream. However, the region of the main flow (seen in the pitch ranges of −0.75 to −0.4 and 0.2–0.65) remains almost unchanged. The location of the peak value in the yaw angle that is observed in the FRAP measurements is expected due to its more downstream lo-

cation. It is also noted that at this more downstream position the pitch range of underturning is broader due to the increased mixing of the vortex into the main flow.

Conclusion

A unique set of steady and unsteady data has been acquired by means of different measurement techniques (3D-PIV and FRAP) in a partially shrouded multistage axial turbine. Owing to the combination of flow velocimetry and pressure measurements, the flow kinematics and loss generation mechanism have been verified. Stereoscopic PIV has been compared with FRAP unsteady pressure measurements and 5HP at the exit of the turbine section, and they show a good agreement.

The interaction of vortex structures has been studied in the interstage tip region. The passage vortex grows downstream of the blade throat and then passes over the shroud platform due to the uncovering of the blade throat. Together with the passage vortex, a vortex is formed due to a sudden flow expansion at the trailing edge of the shroud. The interaction of the two vortex structures entrains low momentum fluid from the wake and thus generates a core of local pressure losses that are measured downstream throughout the interstage region. The analysis of time-distance plots shows that this interaction is triggered by the blade passing period.

Unsteady loss generation has been discussed from the combination of measured relative total pressure and the nondeterministic pressure unsteadiness in the interstage region. Flow structure interaction, with the second stator's leading edge such as vortex stretching and wake bending mechanisms have been observed and found to be a primary source of unsteady losses.

This work presents a unique combination of velocity and pressure data and detailed flow analysis, which enables the possibility to enhance flow modeling used in the design process and provides improved understanding of loss generation mechanisms.

Acknowledgment

Nomenclature

C_{ax} = rotor blade axial chord
Cpt = total pressure coefficient
$(P_{0meas} - P_{Sexit})/(P_{0inlet} - P_{Sexit})$
d = diameter of the seeding particle in Eq. (1)
I = scattered light intensity
I_0 = maximum light intensity in Eq. (1)
Ma = Mach number
NGV = nozzle guide vane
P = static pressure
PS = blade pressure side
SS = blade suction side
u, v, w = axial, tangential, radial flow velocities
T/T_0 = blade passing period fraction
TE = trailing edge
x_0, y_0, z_0 = location of tracer particles in Eq. (1)
z = turbine axial coordinate

Greek

α = angle between cameras A and B
Δz_0 = laser beam thickness
ε = measurement error
β = pitch angle

φ = yaw angle
ρ = density

Subscripts

0 = stagnation quantity
rel = relative quantity
sec = secondary flow vector
mean = mean unit vector

References

[1] Schlienger, J., Kalfas, A. I., and Abhari, R. S., 2005, "Vortex-Wake-Blade Interaction in a Shrouded Axial Turbine," ASME J. Turbomach., **127**, pp. 633–707.
[2] Miller, R. J., Moss, R. W., Ainsworth, R. W., and Horwood, C. K., 2003, "Time-Resolved Vane-Rotor Interaction in a High-Pressure Turbine Stage," ASME J. Turbomach., **125**, pp. 1–13.
[3] Pfau, A., Schlienger, J., Rusch, D., Kalfas, A. I., and Abhari, R. S., 2005, "Unsteady Flow Interaction Within the Inlet Cavity of a Turbine Rotor Tip Labyrinth Seal," ASME J. Turbomach., **127**, pp. 679–688.
[4] Gaetani, P., Persico, G., Dossena, V., and Osnaghi, C., 2006, "Investigation of the Flow-Field on a HP Turbine Stage for Two Stator-Rotor Axial Gaps. Part II: Unsteady Flow Field," ASME Paper No. IGTI GT2006-90556.
[5] Wernet, M. P., 2000, "Application of DPIV to Study Both Steady State and Transient Turbomachinery Flows," Opt. Laser Technol., **32**, pp. 497–525.
[6] Balzani, N., Scarano, F., Riethmuller, M. L., and Breugelmans, F. A. E., 2000, "Experimental Investigation of the Blade-to-Blade in a Compressor Rotor by Digital Particle Image Velocimetry," ASME J. Turbomach., **122**, pp. 743–750.
[7] Sanders, A. J., Papalia, J., and Fleeter, S., 2002, "Multi-Blade Row Interactions in a Transonic Axial Compressor: Part I—Stator Particle Image Velocimetry (PIV) Investigation," ASME J. Turbomach., **124**, pp. 10–18.
[8] Uzol, O., Chow, Y. C., Katz, J., and Meneveau, C., 2002, "Experimental Investigation of Unsteady Flow Field Within a Two-Stage Axial Turbomachine Using Particle Image Velocimetry," ASME J. Turbomach., **124**, pp. 542–552.
[9] Ibaraki, S., Matsuo, T., and Yokoyama, T., 2006, "Investigation of Unsteady Flow Field in Vaned Diffuser of a Centrifugal Compressor," ASME Paper No. GT2006-90268.
[10] Estevadeordal, J., Gogineni, S., Goss, L., Copenhaver, W., and Gorrell, S., 2002, "Study of Wake-Blade Interactions in a Transonic Compressor Using Flow Visualization and DPIV," ASME J. Fluids Eng., **124**, pp. 166–175.
[11] Liu, B., Wang, H., Liu, H., Yu, H., Jiang, H., and Chen, M., 2004, "Experimental Investigation of Unsteady Field in the Tip Region of an Axial Compressor Rotor Passage at Near Stall Condition with Stereoscopic Particle Image Velocimetry," ASME J. Turbomach., **126**, pp. 360–370.
[12] Göttlich, E., Woisetschläger, J., Pieringer, P., Hampel, B., and Heitmeir, F., 2005, "Investigation of Vortex Shedding and Wake-Wake Interaction in a Transonic Turbine Stage using Laser-Doppler-Velocimetry and Particle Image Velocimetry," ASME Paper No. GT2005-68579.
[13] Dorris, A. R., North, W. E., and Malandra, A. J., 1996, "Gas Turbine Blade Having a Cooled Shroud," U.S. Patent No. 5,482,435.
[14] Tomita, Y., 1998, "Gas Turbine Rotor," U.S. Patent No. 5785496.
[15] Nirmalan, N. V., and Bailey, J. C., 2005, "Experimental Investigation of Aerodynamic Losses of Different Shapes of a Shrouded Blade Tip Section," ASME Paper No. IGTI GT2005-68903.
[16] Harvey, N. W., and Ramsden, K., 2001, "A Computational Study of a Novel Turbine Rotor Partial Shroud," ASME J. Turbomach., **123**, pp. 534–543.
[17] Willer, L., Harvey, N. W., Haselbach, F., and Newman, D. A., 2006, "An Investigation Into Novel Turbine Rotor Winglet—Part II: Numerical Results and Experimental Results," ASME Paper No. IGTI GT2006-90459.
[18] Porreca, L., Behr, T., Schlienger, J., Kalfas, A. I., Abhari, R. S., Ehrhard, J., and Janke, E., 2005, "Fluid Dynamics and Performance of Partially and Fully Shrouded Axial Turbines," ASME J. Turbomach., **127**, pp. 668–678.
[19] Prasad, A. K., 2000, "Stereoscopic Particle Image Velocimetry," Exp. Fluids, **29**, pp. 103–116.
[20] Kähler, C. J., Sammler, B., and Kompenhans, J., 2002, "Generation and Control of Tracer Particles for Optical Flow Investigations in Air," Exp. Fluids, **33**, pp. 736–742.
[21] Mellin, A., 1997, "Tracer Particles and Seeding for Particle Image Velocimetry," Meas. Sci. Technol., **8**, pp. 1496–1416.
[22] Zang, W. J., and Prasad, A. K., 1997, "Performance Evaluation of a Scheimpflug Stereocamera for Particle Image Velocimetry," Appl. Opt., **36**, pp. 8738–8744.
[23] Soloff, S. M., Adrian, R. J., and Liu, Z.-C., 1997, "Distortion Compensation for Generalized Stereoscopic Particle Image Velocimetry," Meas. Sci. Technol., **8**, pp. 1441–1454.
[24] Porreca, L., Kalfas, A. I., Abhari, R. S., Yun, Y. I., and Song, S. J., 2006, "Stereoscopic PIV Measurements in A two-Stage Axial Turbine," *The 18th Symposium on Measurement Techniques in Transonic and Supersonic Flow in Cascades and Turbomachinery*, Thessaloniki, Greece, September.
[25] Westerweel, J., Dabiri, D., and Gharib, M., 1997, "The Effect of a Discrete Window Offset on the Accuracy of Cross-Correlation Analysis of Digital PIV Recordings," Exp. Fluids, **23**, pp. 20–28.
[26] Scarano, F., and Riethmuller, M. L., 1999, "Iterative Multigrid Approach in PIV Image Processing With Discrete Window Offset," Exp. Fluids, **26**, pp. 513–523.

[27] Westerweel, J., 1994, "Efficient Detection of Spurious Vectors in Particle Image Velocimetry," Exp. Fluids, **16**, pp. 237–247.

[28] Raffel, M., Willert, C., and Kompenhans, J., 1998, *Particle Image Velocimetry: A Practical Guide*, Springer, Berlin.

[29] Willert, C. E., and Gharib, M., 1991, "Digital Particle Image Velocimetry," Exp. Fluids, **10**, pp. 181–193.

[30] Keane, R. D., and Adrian, R. J., 1992, "Theory of Cross Correlation Analysis of PIV Images," Appl. Sci. Res., **49**, pp. 191–215.

[31] Porreca, L., Hollenstein, M., Kalfas, A. I., and Abhari, R. S., 2007, "Turbulence Measurements and Analysis in a Multistage Axial Turbine," J. Propul. Power, **23**(1), pp. 227–234.

[32] Gizzi, W. P., Roudener, C., Stahlecker, D., Köppel, P., and Gyarmathy, G., 1999, "Time-Resolved Measurements With Fast-Response Probes and Doppler Velocimetry at the Impeller Exit of a Centrifugal Compressor: A Comparison of Two Measurement Techniques," Proc. Inst. Mech. Eng., Part A, **213**, pp. 291–318.

[33] Kupferschmied, P., Köppel, P., Gizzi, W., Roudener, C., and Gyarmathy, G., 1999, "Time-Resolved Measurements in Fast-Response Aerodynamic Probes in Turbomachines," Meas. Sci. Technol., **11**, pp. 1036–1054.

[34] Treiber, M., Kupferschmied, P., and Gyarmathy, G., 1998, "Analysis of the Error Propagation Arising From the Measurements With a Miniature Pneumatic 5-Hole Probe," *XIVth Symposium on Measuring Techniques for Transonic and Supersonic Flows in Cascade and Turbomachines*.

[35] Rosic, B., and Denton, J., 2006, "The Control of Shroud Leakage Loss by Reducing Circumferential Mixing," ASME Paper No. GT2006-90949.

[36] Wallis, A. M., Denton, J. D., and Demargne, A. A. J., 2001, "The Control of Shrouded Leakage Flows to Reduce Aerodynamic Losses in a Low Aspect Ratio, Shrouded Axial Flow Turbine," ASME J. Turbomach., **123**, pp. 334–341.

[37] Yun, Y. I., Porreca, L., Kalfas, A. I., Song, S. J., and Abhari, R. S., 2006, "Investigation of 3D Unsteady Flows in a Two Stages Shrouded Axial Turbine Using Stereoscopic PIV and FRAP—Part II: Kinematics of Shroud Cavity Flow," ASME Paper No. GT2006-91020.

[38] Pullan, G., Denton, J., and Dunkley, M., 2003, "An Experimental and Computational Study of a Streamwise Shed Vortex in a Turbine Stage," ASME J. Turbomach., **125**, pp. 291–297.